RESEARCH ARTICLE

NANO · MICRO small
www.small-journal.com

Computational Discovery of New C—C Coupling Electrocatalysts for CO_2 Electroreduction

Roham Dorakhan, Tiago J. Goncalves, Jehad Abed, Pooya Talebi, Claude Coppex, Mohammadreza Karamad, Ehsan Nikbin, Ali Shayesteh Zeraati, Edward H. Sargent, and Samira Siahrostami**

Catalyst development is key in advancing low-temperature CO_2 electroreduction systems on the path to energy-efficient and low-carbon intensity fuels and chemicals. Much focus lies today on transition metals and their modification, yet a promising avenue remains unexplored—perovskite oxides. Owing to perovskite oxides' distinct electronic structures and reactivity patterns, the systematic screening of these materials can enable identification of new activity regimes and point to mechanisms and active sites distinct from those in traditional transition metal catalysts. Herein, a data-driven search is applied to evaluate the stability of a large library of ≈1500 ABO_3 perovskites at the relevant pH and electrode potentials of CO_2 electroreduction. This study identifies 31 stable candidates and chooses the $ATaO_3$ family of perovskites to synthesize and investigate for its electrochemical performance. Strikingly, C—C coupling is observed with a C_2 Faradaic Efficiency (FE) of 10% at 100 $mAcm^{-2}$ with $KTaO_3$. This study finds the size of the A element in $ATaO_3$ to be critical in C—C coupling, and computational reaction pathway analysis shows a CO^*—$^*CHO$ coupling-driven mechanism for C_2 production. The findings in this study suggest routes to materials design for electrocatalytic C—C coupling on non-copper surfaces.

1. Introduction

The electrochemical CO_2 reduction reaction (CO_2RR) under ambient conditions is a promising approach to produce high-value chemicals and utilize captured CO_2. Copper has been predominantly used as the catalyst enabling production of C_{2+} products, with copper (Cu) alloys having the ability to selectively produce C_2 hydrocarbons.[1–8] The electronic structure of copper allows for optimal CO^* binding, the intermediate necessary for C—C coupling and C_{2+} production, and exhibits suboptimal H^* binding to supress the hydrogen evolution reaction (HER).[9–11]

Copper-based catalysts have seen significant performance improvements since their early use in CO_2RR in 1989; however, stability challenges arising from copper reconstruction, as well as the challenge of tuning its selectivity, remain even 30 years later. The search for new materials that facilitate C—C coupling in CO_2RR is of scientific interest, and indeed recent works[12,13] explore new non-Cu materials capable of C—C coupling, contributing to a growing set of catalytic options as well as mechanistic understanding[14,15].

There are a host of Cu-free catalysts that enable production of C_1 hydrocarbons from CO_2. Oxide-derived lead exhibits a near 100% selectivity toward formate, RuO_2 selectively produces methanol, SnO_x, has been shown to have a promising Faradaic efficiency (FE) toward formic acid and many catalysts such as TiO_2 supported MoS_2 and Ag selectively produce CO.[7,8,14–17] In contrast, there has been little progress in discovery of

R. Dorakhan, E. H. Sargent
Department of Electrical and Computer Engineering
University of Toronto
10 King's College Rd, Toronto, Ontario M5S 3G8, Canada
E-mail: ted.sargent@northwestern.edu

T. J. Goncalves, P. Talebi, C. Coppex
Department of Chemistry
University of Calgary
2500 University Drive NW, Calgary, Alberta T2N 1N4, Canada

J. Abed, E. Nikbin
Department of Materials Science and Engineering
University of Toronto
184 College St, Toronto, Ontario M5S 3E4, Canada

M. Karamad, S. Siahrostami
Department of Chemistry
Simon Fraser University
8888 University Drive, Burnaby, British Columbia V5A 1S6, Canada
E-mail: samira_siahrostami@sfu.ca

A. S. Zeraati
Acceleration Consortium
University of Toronto
700 University Ave, Toronto, Ontario M5G 1X6, Canada

E. H. Sargent
Department of Chemistry
Northwestern University
2145 Sheridan Rd, Evanston, Illinois 60208, United States

The ORCID identification number(s) for the author(s) of this article can be found under https://doi.org/10.1002/smll.202506479

DOI: 10.1002/smll.202506479

Cu-free catalysts producing C—C coupled products. Ag has shown some degree of C—C coupling at elevated pressures, albeit at <100 $mAcm^{-2}$ current densities, while MoS_2 nanoclusters and Ni-based phosphides and oxides have been shown to produce C_{3+} in low current density regimes (<100 $mAcm^{-2}$).[18–20] Perovskites offer a large library of chemical compositions as potential electrocatalysts for CO_2RR that have yet to be systematically screened. The potential of perovskites for producing synthetic fuels and oxygenates was revealed for the first time in 1993, where a copper-containing perovskite ($La_{1.8}Sr_{0.2}CuO_4$) was examined for CO_2RR and showed 80 % FE to methanol, ethanol, and n-propanol at a current density of 180 $mAcm^{-2}$.[21] Since then, there have been limited reports on examining perovskites for CO_2RR. La_2CuO_4 was reported to produce methane, $Sr_2Fe_{1.5}Mo_{0.5}O_6$ to produce CO with an FE of 98%, and $LaInO_3$ to produce formate with an FE of 92%.[22–24] Computational studies on Fe, Co, and Mn perovskites have shown that $GdCoO_3$ and $LaCoO_3$ exhibit similar behaviour in adsorbing CO^* and H^* on Cu, and therefore are suggested to yield similar reaction products.[25]

This study intends to highlight the power of a purely computational screening of a large family of materials for CO_2 electroreduction, that would otherwise be physically exhaustive and unfeasible. We set out to investigate cubic ABO_3 perovskite oxide chemical space (with Pm-3m spacegroup) for suitable catalysts that both enable stable operation under CO_2RR conditions and allow for C—C coupling without the presence of Cu in the catalyst. We implement a computational mega-library search of theory-derived Pourbaix diagrams for perovskites and screen candidates based on their stability under pH/potential regimes relevant to CO_2RR conditions. Through a descriptor-based analysis of activity and selectivity trends, we identify various tantalum-based perovskites ($ATaO_3$) as promising candidates for CO_2RR, where A is Na, K, Rb and Ag. We then conduct mechanistic studies on the alkali metal perovskites $NaTaO_3$, $KTaO_3$, and $RbTaO_3$ as candidates. Next, we synthesize the tantalum-based perovskite materials and conduct CO_2RR experiments under standard reaction conditions. Strikingly, the $KTaO_3$ achieves a 10% FE for C_2 products, with a relative product distribution similar to that obeserved for Cu (ethylene, ethanol, and acetate), as well as >10% methane at industrially relevant current densities (>100 $mAcm^{-2}$). To the best of our knowledge, this represents the first report of Cu-free ABO_3 perovskite catalysts capable of facilitaing C—C coupling (Table S1, Supporting Information). Through various transition state energy computational searches, we show that out of the three candidates, $KTaO_3$ exhibits favourable kinetics for C—C coupling, along with an exergonic pathway for methane production.

2. Results and Discussion

2.1. Computational Search of the Perovskite Material Space for Stable CO_2RR Catalyst Candidates

We start off by searching the perovskite chemical space for materials that are thermodynamically stable under CO_2RR conditions. We select 1500 cubic ABO_3 bulk structures (**Figure 1**) reported in Materials Project database[26] and set the thermodynamic stability to E above Hull (E_Hull) ≤ 0.15 eV to only include structures that are stable with respect to decomposition at the same, fixed composition. This cutoff reflects a balance between stability and the tolerance to small thermodynamic energy fluctuations in bulk perovskites. Of note, surface properties may differ from those of the bulk phase, and that kinetic barriers could prevent the phase transitions of surface structures, as highlighted in previous literature.[26,27] This narrows down the search to ≈500 ABO_3 perovskite.

Next, we identify perovskites stable at pH 8 and 13 (corresponding to −0.47 and −0.77 V versus SHE) to identify alternatives more active than Cu (≈−0.7 V versus SHE overpotential for CO2RR on Cu (211)), excluding those stable only at more negative potentials. For this step, Pourbaix diagram analyzer, Python Material Genome (Pymatgen[28]), and Materials Project[29] were used cooperatively. The potentials of −0.47 and −0.77 V were chosen as thresholds up to which the electrocatalyst should remain stable to survive CO_2RR operating conditions. A reducing potential greater than −0.77 V was deemed inefficient for CO_2RR and would not be desirable when searching for catalysts with superior catalytic activity to copper. The decomposition energy stability threshold was set at 0.25 eV, which is half of the recommended threshold by Persson et al. This value represents a practical cutoff beyond which materials are considered prone to degradation, and it is defined as the difference between the Gibbs free energies of perovskites and the most stable product they decompose to in aqueous media.[30] The most stable decomposition products were determined based on thermodynamic data from reference databases, Materials Project, which adapts DFT calculations, and experimental phase diagrams. Specifically, for the perovskites studied, the decomposition pathways are identified by considering stable hydroxides, oxides, or other competing phases that form under aqueous conditions at pH 8 and 13. This analysis yielded 31 stable perovskites for CO_2RR, of which we shortlisted several candidates for more detailed studies.

Our decision to focus on specific perovskites was driven by a combination of synthesizability and descriptor-based analyses aimed at identifying materials with sufficiently high activity and stability. For example, perovskite materials containing elements such as Sm, Eu, Pr, and Tb were excluded from further investigation due to their rarity, cost, toxicity, and complex synthesis requirements.

Using commonly known CHO^* and CO^* binding energies (BE) as CO_2RR descriptors (Figure 1b) on the $ATaO_3$ family of perovskites, similar characteristics to that of Cu can be observed. Moreover, comparing the CHO^* and CO^* BE to that of H^* (Figure 1c,d), a descriptor for the competing HER reaction, we find a similar propensity toward CO_2RR versus HER, positioning these materials as promising candidates for studying C—C coupling. We selected $NaTaO_3$, $KTaO_3$, and $RbTaO_3$, where the A cation belongs to the alkali metal group in the periodic table, to further investigate their potential for making C_2 products.

We first investigated the stability of these three perovskites against OH^* poisoning. Figure 1e shows the binding energies of CO^* versus OH^* for the examined perovskites, indicating that the $ATaO_3$ family binds OH^* more strongly than Cu does. This finding suggests that while these perovskites may be promising for C—C coupling, OH^* coverage under reaction conditions need further examination. Therefore, we conducted coverage analysis under various pH and potential conditions and identified 0.5 mono layer (ML) OH^* coverage as the most stable. We applied this

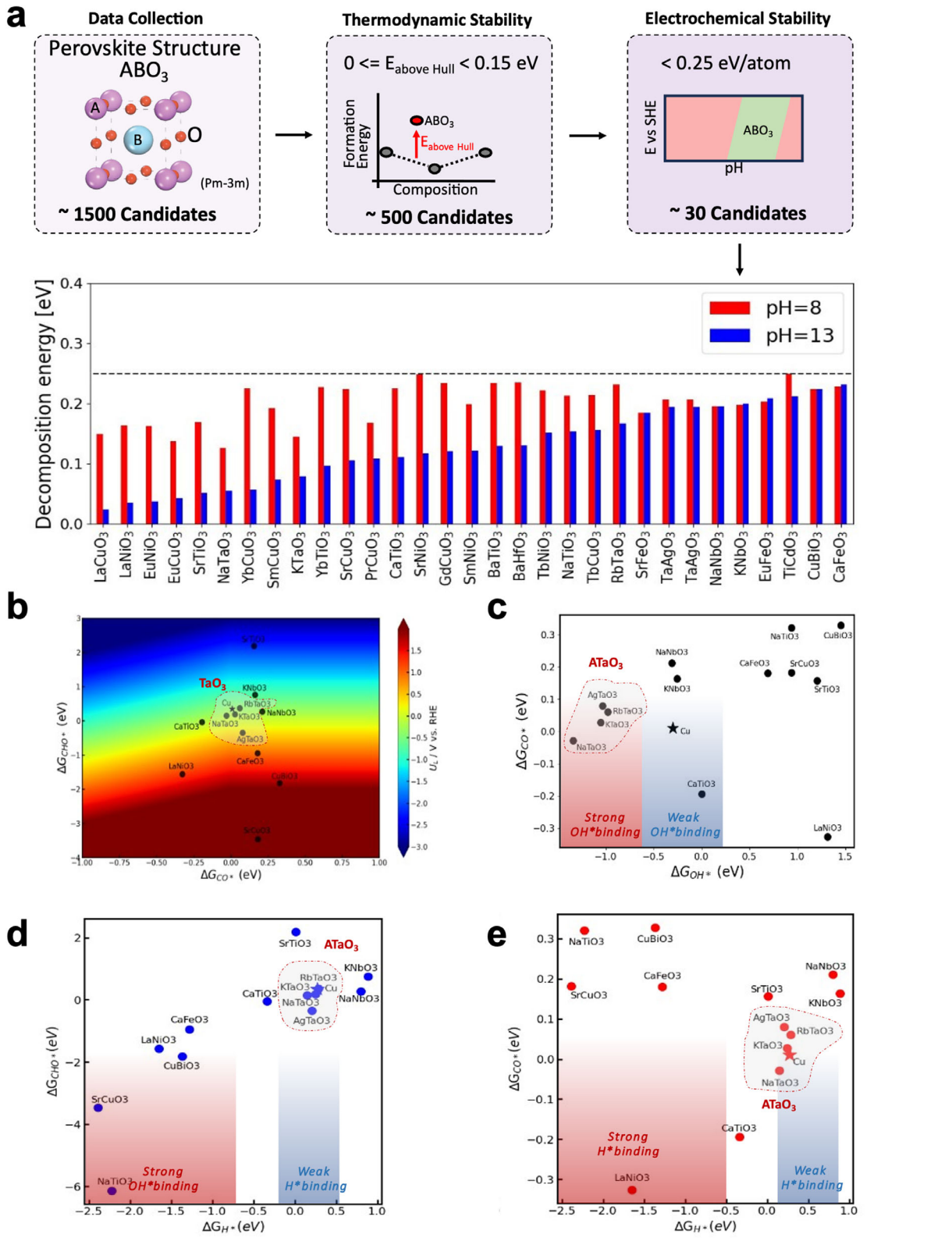

Figure 1. Selection workflow of perovskite material space screening for CO_2RR. a) Selection criteria for the material screening process and the final list of candidate perovskites. b) CHO* and CO*, c) CHO* and H*, d) CO* and H*, e) CO* and OH* binding energy plots of candidate perovskites and Cu. The $ATaO_3$ family of perovskites, particularly $NaTaO_3$, $KTaO_3$, and $RbTaO_3$, show similar binding characteristics to copper and a higher propensity toward CO_2RR versus HER.

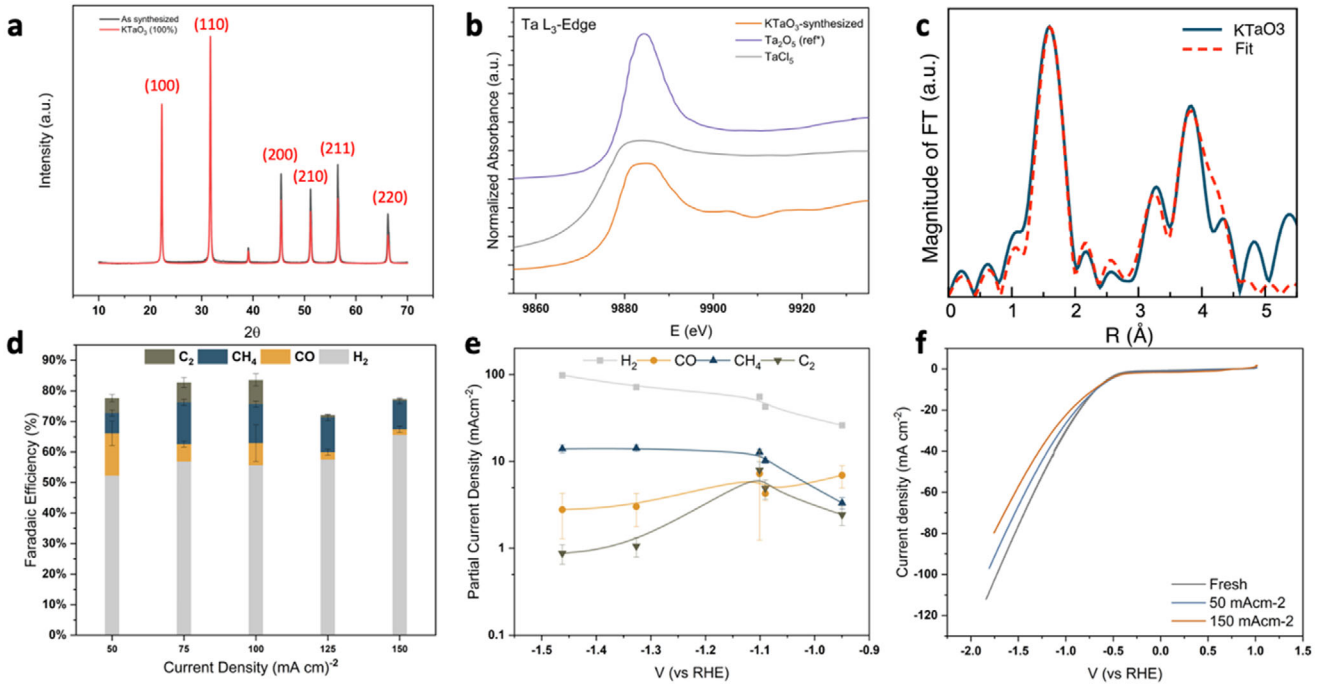

Figure 2. Characterization of synthesized $KTaO_3$ and its electrochemical CO_2 electroreduction. a) XRD diffraction of the as-synthesized $KTaO_3$ samples (black line). The diffraction pattern is compared to standard $KTaO_3$ (red line) taken from database cards #181 838 of the Rigaku NIST ICSD database, b) L_3-edge X-ray absorption near edge structure (XANES) spectra of Ta for $KTaO_3$, $TaCl_5$ and Ta_2O_5 where the Ta_2O_5 spectra has been taken from literature.[31] c) Ta Fourier-transform magnitude of the extended X-ray absorption fine structure (EXAFS) of $KTaO_3$ and its associated fitting. d) Faradaic efficiency of CO_2RR products measured in a flow-cell and 1 M KOH as catholyte e, partial current densities of H_2, CO, CH_4 and C_2 products. f) linear sweep voltammetry (LSV) of the $KTaO_3$ catalyst in a 3 electrode flow-cell using 1 M KOH electrolyte using fresh catalyst and catalyst pretreated under a reductive current of 50 and 150 mA cm^{-2} respectively.

coverage in the computational analysis of $ATaO_3$ perovskites and the mechanistic study of CO_2RR. In our studies, we investigate synthesizable $ATaO_3$ perovskites, ($KTaO_3$ and $NaTaO_3$) experimentally and computationally. In our mechanistic computational investigation, we also studied $RbTaO_3$ and $TlTaO_3$ to investigate the role of the A-site in $ATaO_3$ family of perovskites on CO_2RR activity. Of note is that $TlTaO_3$ did not appear in the most stable shortlisted candidate, due to having a decomposition energy of ≈0.5 eV (still within the threshold suggested by Persson et al.[30])

2.2. Experimental Results

$KTaO_3$ (and $NaTaO_3$, Supporting Information) nanoparticles were synthesized using a one-step hydrothermal process through the reaction of Ta_2O_5 and concentrated KOH.[1,2] The crystal structure of as-synthesized $KTaO_x$ was determined using X-ray Diffraction (XRD) (**Figure** 2a). The XRD pattern confirmed the presence of $KTaO_3$ phase (100 wt.%) (Pm-3m, space group 221) with a perovskite structure. X-ray absorption spectroscopy (XAS) experiments were performed to confirm the structure of the synthesized NPs (Figure 2b and c). L_3-edge XAS spectra indicate the presence of the $KTaO_3$ phase (Figure 2c) and a Ta oxidation state of V+ (Figure 2b). The Fourier- transform of the EXAFS spectra show a first-shell interaction peak at ≈1.6A° assigned to the Ta—O bond, with second shell-Ta-Ta interactions visible in the 3.8–4A° range. Transmission electron microscopy (TEM) imaging shows both nanoparticles in the 200–400 nm range (Figure S1, Supporting Information).

Figure 2d shows the CO_2RR Faradaic efficiency (FE) distribution of the $KTaO_3$ catalyst. Under CO_2 electroreduction conditions, the catalyst shows 9% FE toward CO_2RR with 1 mg cm^{-2} loading at 100 mA cm^{-2} and This value increases to ≈14% when the loading is increased to 5 mg cm^{-2} (Figure S2, Supporting Information). Using the same optimized loading but under CORR conditions, the catalyst can provide 15.5% FE toward CORR products (Figure S3, Supporting Information). While the predominant CO_2RR product was CH_4, a consistent amount of C_2 products were also observed at all current densities studied. The observed C—C coupling products were ethylene, ethanol and acetate, a similar product distribution to that found on Cu. Looking at the partial current densities of the CO_2RR products (Figure 2e), the CH_4 and C_2 exhibit a positive Tafel slope in the lower potential regime (−0.9 to −1.1 versus RHE), indicative of an electron-transfer rate-determining step (ET-rds). The potential dependence of C_2 products becomes negative at higher potential, while that of CH_4 is nearly zero, both indicating that the ET-rds is no longer plausible. The CO partial current density however, has a negative potential dependence in all potential regimes. We conclude that the CO* coverage on the $KTaO_3$ is very limited, where an increase in current density allows for a proton-coupled electron transfer (PCET) to occur on the CO*, producing CHO*. If the CO* coverage is sufficiently high, the CHO* can undergo

C—C coupling with the CO*, producing the C_2 products, or if the CO* is too low, e.g., <−1.1 V versus RHE, it will undergo complete protonation and produce CH_4.

To further investigate the mechanism of C—C coupling in these perovskite systems, we measured the activity of $NaTaO_3$ nanoparticles synthesized using the same method (Figure S4, Supporting Information). No detectable amount of C_2 products were measured under any potential, signifying the importance of the potassium element (A element in $KTaO_3$) in enabling the C—C coupling step.

We also investigated the effect of reductive pre-treatment on the performance of the catalyst. Figure 2f shows the linear sweep voltammetry (LSV) for the fresh $KTaO_3$ sample, along with samples pre-treated under reductive currents of 50 and 150 mA cm^{-2} during reaction conditions. Higher reductive current treatments lower the activity of the catalyst, presumably due to changes in the oxide structure under highly reductive potential (Figure S5, Supporting Information). This confirms the active sites to be oxide in nature. Isotope labelling experiments using ^{13}CO showed CO to be the reacting carbon species (Figure S6, Supporting Information). Stable operation was achieved in a flowcell electrolyzer, with little to no drop in ethylene FE (Figure S7, Supporting Information). X-ray photoelectron spectroscopy (XPS) revealed no change in the Ta electronic structure of $KTaO_3$ catalyst following CO_2 electroreduction (Figure S8, Supporting Information). The XPS also revealed Ta^{5+} as the sole Ta species before and after the reaction, pointing to the stability of the catalyst throughout the reaction.

$KTaO_3$ presents (to our extent of knowledge) the first copper-free perovskite oxide to facilitate C—C in both CO_2 and CO electroreduction conditions, having both favorable electronics to allow CO^* and CHO^* adsorption, and favorable interatomic adsorbent distance to allow for C—C coupling. To elucidate the C—C coupling mechanism on $KTaO_3$, DFT calculations were performed to investigate various CO_2RR pathways leading to methane, methanol, ethylene and ethanol.

2.3. Computationally Derived Mechanistic Results

The propensity of perovskites toward partial reduction at negative potentials was evaluated prior to performing the mechanistic study. To assess this, the stability of $KTaO_3$ (as an example) was tested against surface oxygen reduction and oxygen vacancy formation under CO_2RR conditions (see supplementary note 1 for more details). Table S2 (Supporting Information) shows the potential required to reduce surface oxygen atoms to water on A and B-terminated $KTaO_3$ (100) surface at pH 8 and 13 as examples. $KTaO_3$ catalyst remains stable against partial reduction only if the CO_2RR occurs at more positive potentials than the potential required to reduce surface oxygen atoms. This analysis shows that surface oxygen reduction on A-termination of $KTaO_3$(100) readily occurs at relevant CO_2RR potentials, while for B-termination of $KTaO_3$(100), very large negative potentials, e.g., close to −2.5 V and −5.8 at pH 8 and 13, respectively, are required to reduce surface oxygen atoms. Thus, we only focus on the B-terminated $KTaO_3$(100), which shows high stability against partial reduction under CO_2RR conditions and fully evaluate its catalytic activity using DFT calculations. Moreover, since the relative stability of different CO_2RR intermediates at the surface can drastically change the surface chemistry, we calculated the equilibrium coverages (Figure S9, Supporting Information) for a wide range of intermediates under CO_2RR conditions. Based on these findings, $KTaO_3$ has the highest stability for 0.5 ML of $^*OH$ (illustration in the bottom-right corner of **Figure 3a**) for potential windows of −0.5 V and above at pH 8 and 13, which was used as the equilibrium surface coverage for the mechanistic study.

Figure 3a displays different CO_2RR pathways to form methane, methanol, ethylene, and ethanol, and Figure 3b shows the minimum energy pathways. The conversion of CO_2 (shown in Figure 3a–c) starts with its reduction to $COOH^*$. The reduction through proton-coupled electron transfer (PCET) may either happen by reducing the OH tail of $COOH^*$, promoting the splitting of the carbon–oxygen bond and the formation of carbon monoxide plus water, or reducing carbon, leading to the formation of formic acid ($HCOOH^*$). Our mechanistic study shows surface-bound formic acid and formyl (CHO^*) are more stable than the desorption of formic acid or the formation of CO by at least 0.2 eV, indicating that the pathway to form formyl, the first relevant intermediate in the C—C coupling, is more likely to occur than the release of the first C_1 products (carbon monoxide or formic acid). Despite other C_1 products (MeOH and CH_4) being more likely to form at U_{RHE} = 0.0 V due to having more stable reaction free energies than the C—C coupling pathways, at lower applied potentials (U_{RHE} = − 0.45 and − 0.7 V) ethene and ethanol pathways become increasingly more favorable.

Various intermediates (OC^*—$^*CHO$, OHC^*—$^*CHO$ (Figure S10, Supporting Information), OHC^*—$^*CH_2O$ (Figure S11, Supporting Information), OH_2C^*—$^*CH_2O$ (Figure S12, Supporting Information), and H_3C^*—$^*CHO$ (Figure S13, Supporting Information)) were chosen to study the C—C coupling, as the transition-state energy (barrier) heavily depends on which intermediates are coupled together. We observe that the smallest C—C coupling barrier corresponds to the OC^*—$^*CHO$ coupling, with a barrier height of 0.57 eV (Figure 3a,b green pathway), followed by the coupling of OHC^*—$^*CHO$, OHC^*—$^*CH_2O$ and OH_2C^*—$^*CH_2O$, with barriers of 0.61 eV (Figure 3a,b, red pathway), 0.84 eV (Figure 3a,b, orange pathway) and 1.76 eV (Figure 3a,b, blue pathway). This finding demonstrates that the C—C coupling mechanism goes through the same critical step as the one on copper, resulting in similar product distribution, which is consistent with our experimental observation. After the C—C coupling, the first C_2 intermediate is further reduced to form either ethylene or ethanol.

We note that kinetic rates of reaction are limited to the height of the steps' internal barriers and that higher applied voltages than those shown here do not improve product formation. An example is shown in the least energetic C—C coupling pathway, Figure 3c, where different potentials significantly lower the Gibbs free energies of intermediate steps, but the internal barrier remains unchanged. This is due to the C—C barrier being a purely thermochemical process. Gibbs free energies at different applied voltages (versus RHE) for the alternative pathways are shown in Figures S10–13 (Supporting Information). Based on these calculations, we confirm that $KTaO_3$ has a reasonable rate for CO_2 reduction to methane and ethylene. We also note that ethanol formation is highly competitive with ethylene formation because their formation energies are thermoneutral.

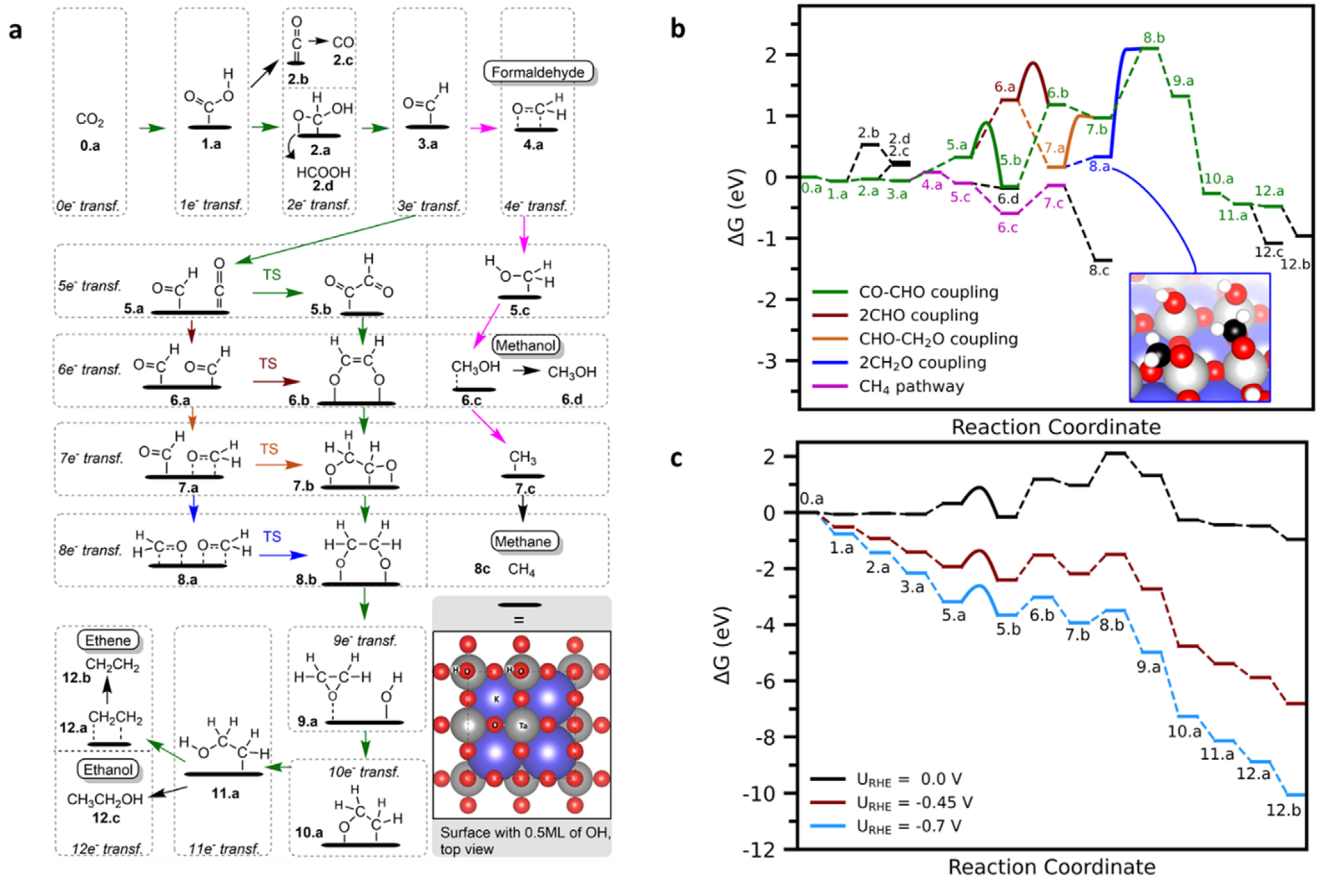

Figure 3. Mechanistic landscape of CO_2RR on $KTaO_3$. a) Reaction mechanism scheme showing different pathways of the CO_2 reduction to C_1 and C_2 products, namely methane, methanol, ethene, and ethanol. The illustration of $KTaO_3$ surface (top view) is shown at the bottom-right corner of the scheme, with 0.5 ML of OH molecules that exhibit highest stability when compared to other adsorbates. b) Gibbs free energy profile of the reaction pathway involving the carbon-carbon coupling using different intermediates (2CHO, $2CH_2O$, CHO—CH_2O, and CO—CHO) at 0 V (versus RHE) and 300 K. The formation of methane and methanol are also shown in this diagram, pathway in magenta, as well as ethanol, which is formed prior to ethylene. Products are depicted in black, and intermediates are color-coded according to their assigned pathway. On the carbon–carbon coupling, a few intermediates on different pathways overlap. c) Gibbs free energy profile for the carbon–carbon coupling via CO^*—$^*CHO$ interactions, exhibiting the lowest barrier compared to alternative pathways, at different applied voltages (versus RHE). The mechanism illustrates a general proton-coupled electron transfer (PCET) process, and all thermodynamic data are referenced to RHE. Reaction coordinates in graphs b and c do not necessarily depend on the number of ($H^+ + e^-$) transferred to the system since thermodynamic processes, such as the C—C coupling kinetic barrier, are also investigated.

We further investigated C—C coupling via a prior H-transfer between surface–adsorbed $^*CH_3$ and $^*CHO$. This hydrogen transfer from $^*CH_3$ is highly energetic, with an internal barrier approaching 2 eV (Figure S13, Supporting Information), reflecting the surface's limited ability to break C—H bonds at room temperature, similar to observations on Cu surfaces.[32] The DFT-converged adsorbation configurations of C1 and C2 intermediates along with configurations of transition states are shown in Figures S14–S16, Supporting Information.

To gain deeper insight into the behavior of $ATaO_3$ perovskites, the mechanisms for C_1 and C_2 products formation were evaluated on three other perovskites, $NaTaO_3$, $RbTaO_3$, and $TlTaO_3$ (Figure S17a,b, Supporting Information). DFT calculations show that $NaTaO_3$ is incapable of maintaining the OC^*—$^*CHO$ couple stable at the surface. As a result, C—C coupling is unlikely to occur, and only C_1 products are formed. On the other hand, the kinetic rates of formation of C_1 products (methane or methanol) are expected to be similar to that of $KTaO_3$, with intermediate free energies differing by up to 0.1 eV. This corroborates the lack of C_2 products observed on $NaTaO_3$ as discussed in the experimental section and the importance of A's atomic radius in $ATaO_3$ perovskite families for C—C coupling.

To further investigate the role of the A-cation size in C—C coupling, the mechanism for C—C coupling and the trend in free energies of different CO_2RR intermediates were further studied on $RbTaO_3$ and $TlTaO_3$, belonging to the same family of perovskites with similar B sites. Both $RbTaO_3$ and $TlTaO_3$ follow similar mechanisms to $KTaO_3$ for C—C coupling via OC^*—$^*CHO$ intermediate (Figure S17, Supporting Information). Intermediates such as $OHC—CH_2O^*$, $OH_2CCH_2O^*$, and $^*CH_2CH_2O$+OH^* are more energetically stable on $TlTaO_3$ (≈1 eV), making it another promising catalyst beyond copper for C_2 production. However, due to thallium's toxicity, we avoided synthesizing and testing this material experimentally. $RbTaO_3$, also follows the same mechanism for C—C coupling (Figure S18, Supporting Information) but the reduction of $^*OCCHO$ to $^*OHCCHO$

intermediate is highly energetic compared to the other perovskites, requiring much higher applied potentials ($OC^*—^*CHO$ intermediate, Figures S17b,S18 and S19, Supporting Information) potentially limiting the feasibility of $RbTaO_3$ for C_2 production. We also note that $RbTaO_3$ has a rather unstable $HCOOH^*$ intermediate energy compared to the other tantalates, indicating that the catalyst might be inefficient in the synthesis of even C_1-relevant products. Synthesis of $RbTaO_3$ was not successful using the methodology used for $KTaO_3$ and $NaTaO_3$, and hence, future work would require investigating synthesis methods to produce this material and its potential application in CO_2RR.

Finally, we note that explicit electric fields and electrolyte ions were not included in our DFT calculations. While these factors are known to affect adsorption energetics—particularly polarizable intermediates involved in C—C coupling—their incorporation requires extensive sampling of diverse configurations at the perovskite-solution interface.[33] Given the structural complexity and chemical variability of perovskite surfaces, identifying representative ensembles of solvent molecules and ion distributions remains a nontrivial challenge. Addressing these effects would constitute a substantial and independent study beyond the scope of the present work. To better simulate the electrochemical interface in future studies, more advanced modeling frameworks could be adopted, including: 1) Implicit solvation models (e.g., VASPsol) to approximate the dielectric environment of the electrolyte; 2) The Solvated Jellium Model (SJM), which incorporates a continuum electrolyte and allows for tuning of the electrode potential under constant-potential conditions [34]; and 3) Constant-potential DFT methods, such as those implemented in the Grand Canonical DFT framework,[35] which more accurately capture the behavior of charged interfaces under operating bias.

3. Conclusion

Based on the screening of a large database of perovskites, the most stable were chosen to investigate CO_2RR. Various C—C coupling pathways were investigated on $KTaO_3$, $NaTaO_3$, $RbTaO_3$, and $TlTaO_3$. Amongst these, $KTaO_3$ demonstrated low C—C coupling barriers and favorable energetics for C_2 product formation at low applied potentials. According to the Sabatier principle, this means that the binding energies are optimally balanced, not too strong nor too weak, promoting efficient CO_2RR. The perovskite oxide was synthesized and showed significant activity toward C—C coupling under CO_2RR and CORR conditions, producing ≈10% C_2 hydrocarbons such as ethylene, ethanol, and acetate. We calculated the C—C coupling transition state energy in detail on a set of reaction intermediates on $KTaO_3$ to model reaction pathways of the formation of ethylene and ethanol. The size of the intermediates involved in the C—C coupling affects the intrinsic barrier, rendering the reaction progressively more hindered the larger the molecules are. Therefore, the coupling between intermediates is kinetically faster the sooner it occurs, i.e., before further reduction steps. We found $CO^*—^*CHO$ coupling to have an intrinsic barrier of only 0.57 eV, compared to $OHC^*—^*CHO$ (0.61), $OHC^*—^*CH_2O$ (0.84), and $OH_2C^*—^*CH_2O$ (1.76). Among Na, K, and Rb, which are listed as the most stable perovskites from our initial screening analysis, only K has the most optimal reaction energy profile for C—C coupling. This is strongly related to its electronic structure characteristics, such as optimal binding energies toward CO_2 intermediates and the size of the A cation. Smaller A-cations like Na failed to facilitate C_2 product formation, whereas larger A cations such as K, Rb, and Tl appeared to promote C—C coupling, due to the optimal distance between active sites.

4. Experimental Section

Computational Details: Atomic Simulation Environment (ASE) was used to handle the structures generation.[36] All electronic structure calculations were done using the Quantum ESPRESSO program package.[37,38] Core electrons were approximated using the GBRV ultrasoft pseudopotentials.[39] The non-linear core corrected and scalar relativistic ultrasoft pseudopotentials was taken from the Quantum ESPRESSO library. The Perdew–Burke–Ernzerhof (PBE) was used as the exchange-correlation functional with zero damping Grimme's dispersion corrections included.[40–44]

The electron wavefunctions were expanded in plane waves up to a cutoff energy of 50 Ry, while the electron density is represented on a grid with an energy cutoff of 500 Ry. The Brillouin zone was sampled using a (5 × 5 × 1) Monkhorst-Pack grid. The bulk structures of cubic (Pm-3m) ABO_3 Perovskites were obtained from the Materials Project database and reoptimized with our calculation setup. The (100) facet, which has the lowest surface energy and a 2 × 2 unit-cell slab model with 4-layers thickness was constructed. Only the top two layers and the adsorbates were allowed to relax. A vacuum of 18 Å was used in the z-direction to avoid interaction between the periodic images. Moreover, to remove spurious interaction between the periodic images a dipole correction was applied. The BFGS algorithm[45–48] was used for geometry optimization with the convergence thresholds for the energy and force set to 1×10^{-9} Ry and 4×10^{-4}, Ry/bohr (1×10^{-2} eV $\forall^{-1}$), respectively. Vibrational frequencies were computed using the rigid rotator and oscillator, and harmonic approximation with a finite-difference scheme, to obtain the entropic contribution to the free energies. Transition states were computed with ARPESS [49] and were ensured to have only one imaginary frequency, which corresponds to the vibrational mode of the reaction.

The computational hydrogen electrode (CHE) model was used to calculate the free energy levels of all adsorbates. In this model, the free energy change of each electrochemical reaction step that involves an electron–proton transfer is calculated referring to the reversible hydrogen electrode (RHE), where the chemical potential of an electron–proton pair is equal to that of half of hydrogen in the gas phase at standard conditions. The electrode potential is taken into account by shifting the electron energy by −eU where e and U are the elementary charge and the electrode potential, respectively. The limiting potential is defined as the negative of the maximum free energy difference between any two successive electrochemical steps. Moreover, the free energies of adsorption, ΔG_{DFT} at standard conditions of pressure and temperature is calculated as below:

$$\Delta G_{DFT} = \Delta E_{DFT} + \Delta ZPE - T\Delta S \quad (1)$$

where ΔZPE and TΔS are the difference between the zero-point energy and entropy of reactants and products, respectively.

All slabs simulated in the study are stoichiometrically balanced, with a zero net charge per supercell. To achieve this, different terminations are used for the top and bottom of the slab, e.g. top is Ta terminated while bottom is K, which result in a dipole within the slab. The in-slab dipole is then neutralized by including dipole corrections and eliminating any self-interaction within the slab.

The Pourbaix Diagram Analyzer in Materials Project, [26,50–52] was used to generate Pourbaix diagrams, i.e., phase diagrams that depict the stable phases of perovskites as a function of pH and electrochemical potential (voltage). This computational tool leverages thermodynamic data to predict the electrochemical stability of perovskites in aqueous environments under various pH and electrode potential. It relies primarily on VASP calculations for formation energies and leverages multiple techniques to

approximate dynamic effects such as solvation and pH changes. These techniques involve using thermodynamic data from DFT, where VASP calculations provide the Gibbs free energies of various compounds in their standard states (solid, liquid, or gas), obtained from the electronic ground-state energies computed in the DFT calculations. It then includes solvation effects via empirical or semi-empirical corrections to account for the interaction of species with the solvent (usually water). For ions and aqueous species, solvation free energies are often taken from experimental data or computed using continuum solvation models like the Polarizable Continuum Model (PCM). The pH of the solution is considered via affecting the chemical potential of protons (H^+ ions). The Nernst equation is used to relate the electrochemical potential to pH. For a given reaction, the Gibbs free energy change is adjusted based on the pH, allowing for calculating stability as a function of pH.

Synthesis Details: $KTaO_3$ nanoparticles were synthesized using one-step hydrothermal process through the reaction of Ta_2O_5 and concentrated KOH 1,2. First, 16 g of KOH was dissolved in 24 mL of DI water then 4.4 g of Ta_2O_5 4.4 g and 1.2 mL of PEG-400 were added to the solution. The mixture was stirred for 1 h on a magnetic stirrer at room temperature to produce a homogeneous suspension. Afterward, the suspension was transferred into a 50 mL Teflon-lined stainless-steel autoclave and then sealed and heated at 200 °C for 24 h. After being cooled in air to room temperature, the precipitates were washed several times with DI water by centrifuging in 50 mL tubes until the pH value of the solution was close to 7. The solid in the bottom of the centrifuge tube was dried in an oven at 60 °C for 24 h, and the final white $KTaO_3$ powder was collected for experiments.

X-Ray characterization: A Miniflex 600 (Rigaku, Japan) equipped with D/tex Ultra silicon trip detector and Cu Kα radiation (λ = 1.5418 Å) was used. Powders were prepared by mixing with methanol and then dropping a small drop of the mixture to fill a 4 mm diameter x 100 µm deep groove in a single-crystal silicon holder (zero-background). The angle varied between 20° and 60° with a step size of 0.05° and a scan rate of 10° min^{-1} for highly crystalline samples and 1° min^{-1} for nanocrystalline samples.

Transmission Electron Microscopy: A high-resolution field emission transmission electron microscope (HF3300, Environmental-CFE-TEM) was employed to obtain STEM images and conduct EDS elemental mapping of the samples.

Gas Diffusion Electrode (GDE) Reparation: Gas diffusion electrodes (GDE) were prepared using a Freudenberg H23C9 carbon paper with a PTFE treated microporous layer (Fuel cell store). The $KTaO_3$ nanoparticles were dispersed in 4–6 mL of methanol along with a Nafion dispersion (5 wt.% in ethanol, EW = 1000, D520 Fuel cell store) with a 5 $\mu L/mg_{KTaO3}$ ratio. The nominal nanoparticle loading was 1-15 mg cm^{-2}. The dispersion was sonicated for a minimum of 1 h, until all the particles were fully dispersed and did not precipitate over the course of the spray application. The dispersion was then spray-coated on the carbon paper using an airbrush (Paasche H-series). The samples were left to dry overnight (>12 h) before being subjected to electrochemical testing in a flow cell.

Electrochemical CO_2 and CO Reduction Experiments: Electrochemical rate measurements were performed a flow cell configuration. The catalyst deposited GDE was used as the working electrode (cathode) and Pt mesh (2 x 2 cm^2, 0.06 mm mesh, Sigma–Aldrich) as the counter electrode (anode). A bipolar membrane (Fumasep FBM Bipolar membrane) was used to separate the anodic and cathodic compartments. The flow cell assembly constituted the GDE, anion exchange membrane, and Pt anode, while liquid electrolyte (1 –M KOH, Sigma Aldrich) was circulated in both anodic and cathodic compartments using a peristaltic pump (McMaster-Carr). Carbon monoxide (Praxair, Grade 2.5) was passed behind the GDE using a mass flow controller (Sierra SmartTrack 100). An Ag/AgCl reference electrode was utilized for half-cell potential measurement. Electrochemical reactions were performed using an electrochemical workstation (Autolab PGSTAT302N) connected to a current booster (Metrohm Autolab, 10 A). Electrode potentials were rescaled to the RHE reference by:

$$E_{VsRHE} = E_{VsAg/AgCl} + 0.235V + 0.059 \times PH \quad (2)$$

An electrochemical impedance spectroscopy (EIS) measurement using an Autolab PGSTAT302N electrochemical workstation was performed to obtain a cell resistance of 3.60 Ω. iR corrections to the potential were then performed using the following equation:

$$E_{iR-free} = E_{VsAg/AgCl} - 0.85 R_{cell} i_{cell} \quad (3)$$

where $E_{iR\text{-}free}$ is the corrected potential at the cathode, $E_{Vs\ Ag/AgCl}$ is the applied potential, and i_{cell} is the total current (a negative value at the cathode). A correction factor of 0.85 is used due to the 1 M KOH electrolyte's high conductance and low voltage drop across the electrolyte.

The cell is routinely washed with a 1 M H_2SO_4 solution to remove any contamination, followed by a wash with DI water for a minimum of 3 times. Following each wash, a GDE without catalyst (only H23C9) was inserted into the electrode and the CO_2RR products measured. The cell would be washed until H_2 was the sole observable product, indicating the lack of metallic contamination in the system.

Product Analysis: The gas products were sampled with an air-tight syringe (Hamilton, 5 mL). The gas sample was injected into a gas chromatograph (Shimadzu GC-2014) equipped with a thermal conductivity detector (TCD) and a flame ionization detector (FID). A Molecular Sieve 5A and Carboxen-1000 column were installed upstream from the TCD and FID, respectively to separate the H_2, CO, and gaseous hydrocarbons. The liquid products were quantified using nuclear magnetic resonance spectroscopy (NMR). 1H NMR spectra of the analyte samples were taken using an Agilent DD2 600 spectrometer with dimethyl sulfoxide (DMSO) as an internal standard. Faradaic efficiency (FE) of the gas product was calculated by the following equation:

$$FE_{i,\,gas} = y_{i,\,g} \dot{V} z_i F \frac{P_0}{RT} j_{total} \quad (4)$$

where y_i is the volume fraction of gas product i, V is the outlet gas flow rate in sccm, z_i is the number of electrons associated with producing one molecule of i, F is the Faraday constant, P_0 is atmospheric pressure, R is the ideal gas constant, T is the temperature, and j_{total} is the total current density. The FE of liquid product was calculated using the following equation:

$$FE_{i,liquid} = n_{i,liquid} z_i F \frac{1}{Q_{total}} \quad (5)$$

where n_i is the number of moles of liquid product i, and Q is the total charge passed prior to the liquid sample being taken.

Gas products were collected in 5 min intervals until a stable performance was reached. Liquid products were collected after 20 min of continued electrolysis. Each experiment was running for a period of 40–120 min to ensure stable operation and consistent data acquisition.

X-Ray Photoelectron Spectroscopy: The XPS was conducted using a Perkin-Elmer 5600 device utilizing a monochromatic aluminum X-ray source.

Electrochemical Characterization: Cyclic voltammetry characterization with electrodes assembled in a flow cell was performed with the same equipment used for CORR experiments. iR correction of the applied potential was not performed.

Supporting Information

Supporting Information is available from the Wiley Online Library or from the author.

Acknowledgements

R.D., T.J.G., and J.A. contributed equally to this work. E.H.S. acknowledges the support of this work by the Ontario Research Foundation—Research

Excellence Program (no. ORF-RE08-034, E.H.S.) and the Natural Sciences and Engineering Research Council (NSERC) of Canada (no. RGPIN-2017-06477, E.H.S). S.S. acknowledges the support from the Natural Sciences and Engineering Research Council (NSERC) of Canada (Discovery Grant No. RGPIN-2023-05298). The computational research was supported by resources provided by the Digital Research Alliance of Canada (www.alliancecan.ca).

Conflict of Interest

The authors declare no conflict of interest.

Data Availability Statement

The data that support the findings of this study are available from the corresponding author upon reasonable request.

Keywords

catalysis, CO_2RR, DFT, electrocatalysis, energy, materials discovery

Received: July 3, 2025
Revised: August 20, 2025
Published online:

[1] F. Pelayo García de Arquer, C.-T. Dinh, A. Ozden, J. Wicks, C. McCallum, A. R. Kirmani, D.-H. Nam, C. Gabardo, A. Seifitokaldani, X. Wang, Y. C. Li, F. Li, J. Edwards, L. J. Richter, S. J. Thorpe, D. Sinton, E. H. Sargent, *Science* **2020**, *367*, 661.
[2] J. E. Huang, F. Li, A. Ozden, A. Sedighian Rasouli, F. Pelayo García de Arquer, S. Liu, S. Zhang, M. Luo, X. Wang, Y. Lum, Y. Xu, K. Bertens, R. Kai Miao, C.-T. Dinh, D. Sinton, E. H. Sargent, *Science* **2021**, *372*, 1074.
[3] W. Ma, S. Xie, T. Liu, Q. Fan, J. Ye, F. Sun, Z. Jiang, Q. Zhang, J. Cheng, Y.e Wang, *Nat. Catal.* **2020**, *3*, 478.
[4] X. Wang, Z. Wang, F. P. G. de Arquer, C. T. Dinh, A. Ozden, Y. C. Li, D.-H. Nam, J. Li, Y. S. Liu, J. Wicks, Z. Chen, M. Chi, B. Chen, Y. Wang, J. Tam, J. Y. Howe, A. Proppe, P. Todorović, F. Li, T.-T. Zhuang, C. M. Gabardo, A. R. Kirmani, C. McCallum, S. F. Hung, Y. Lum, M. Luo, Y. Min, A. Xu, C. P. O'Brien, B. Stephen, et al., *Nat. Energy* **2020**, *5*, 478.
[5] M. Luo, Z. Wang, Y. C. Li, J. Li, F. Li, Y. Lum, D.-H. Nam, B. Chen, J. Wicks, A. Xu, T. Zhuang, W. R. Leow, X. Wang, C.-T. Dinh, Y. Wang, Y. Wang, D. Sinton, E. H. Sargent, *Nat. Commun.* **2019**, *10*, 5814.
[6] W. Liu, P. Zhai, A. Li, B. Wei, K. Si, Y. Wei, X. Wang, G. Zhu, Q. Chen, X. Gu, R. Zhang, W. Zhou, Y. Gong, *Nat. Commun.* **2022**, *13*, 536.
[7] A. Bhowmik, H. A. Hansen, T. Vegge, *J. Phys. Chem. C* **2017**, *121*, 18333.
[8] M. Karamad, H. A. Hansen, J. Rossmeisl, J. K. Nørskov, *ACS Catal.* **2015**, *5*, 4075.
[9] T. K. Todorova, M. W. Schreiber, M. Fontecave, *ACS Catal.* **2020**, *10*, 1754.
[10] Y. J. Zhang, V. Sethuraman, R. Michalsky, A. A. Peterson, *ACS Catal.* **2014**, *4*, 3742.
[11] R.-Z. Zhang, B.-Y. Wu, Q. Li, L.-L. Lu, W. Shi, P. Cheng, *Coord. Chem. Rev.* **2020**, *422*, 213436.
[12] Y. Zhou, A. J. Martín, F. Dattila, S. Xi, N. López, J. Pérez-Ramírez, B. S. Yeo, *Nat. Catal.* **2022**, *5*, 545.
[13] L. R. L. Ting, D. R. García-Muelas, D. A. J. Martín, F. L. P. Veenstra, S. T.-J. Chen, Y. Peng, E. Y. X. Per, S. Pablo-García, N. López, J. Pérez-Ramírez, B. S. Yeo, *Angew. Chem., Int. Ed.* **2020**, *59*, 21072.
[14] L. Yu, Y. Xie, J. Zhou, Y. Li, Y. Yu, Z. Ren, *J. Mater. Chem. A* **2018**, *6*, 4706.
[15] Y. Chen, M. W. Kanan, *J. Am. Chem. Soc.* **2012**, *134*, 1986.
[16] E. Tayyebi, J. Hussain, E. Skúlason, *Chem. Sci.* **2020**, *11*, 9542.
[17] S. Mezzavilla, Y. Katayama, R. Rao, J. Hwang, A. Regoutz, Y. Shao-Horn, I. b. Chorkendorff, I. E. L. Stephens, *J. Phys. Chem. C* **2019**, *123*, 17765.
[18] S. J. Raaijman, M. P. Schellekens, P. J. Corbett, M. T. M. Koper, *Angew. Chem., Int. Ed.* **2021**, *60*, 21732.
[19] X. Zhong, H.-J. Peng, C. Xia, X. Liu, *J. Mater. Chem. A* **2024**, *12*, 19663.
[20] H. Zhang, Y. Xu, M. Lu, X. Xie, L. Huang, *Adv. Funct. Mater.* **2021**, *31*, 2101872.
[21] M. Schwartz, R. L. Cook, V. M. Kehoe, R. C. MacDuff, J. Patel, A. F. Sammells, *J. Electrochem. Soc.* **1993**, *140*, 614.
[22] Y. Zhu, W. Zhou, Z. Dong, X. Zhang, Z. Chen, Z. Liu, F. Li, J. Fan, M. Jiao, L. Liu, *J. CO2 Util.* **2023**, *68*, 102342.
[23] H. Lv, L. Lin, X. Zhang, D. Gao, Y. Song, Y. Zhou, Q. Liu, G. Wang, X. Bao, *J. Mater. Chem. A* **2019**, *7*, 11967.
[24] S. Chen, Y. Su, P. Deng, R. Qi, J. Zhu, J. Chen, Z. Wang, L. Zhou, X. Guo, B. Y. Xia, *ACS Catal.* **2020**, *10*, 4640.
[25] J. Hwang, K. Akkiraju, J. Corchado-García, Y. Shao-Horn, *J. Phys. Chem. C* **2019**, *123*, 24469.
[26] A. Jain, S. P. Ong, G. Hautier, W. Chen, W. D. Richards, S. Dacek, S. Cholia, D. Gunter, D. Skinner, G. Ceder, K. A. Persson, *APL Mater.* **2013**, *1*, 11002.
[27] S. P. Ong, W. D. Richards, A. Jain, G. Hautier, M. Kocher, S. Cholia, D. Gunter, V. L. Chevrier, K. A. Persson, G. Ceder, *Comput. Mater. Sci.* **2013**, *68*, 314.
[28] S. P. Ong, W. D. Richards, A. Jain, G. Hautier, M. Kocher, S. Cholia, D. Gunter, V. L. Chevrier, K. A. Persson, G. Ceder, *Comput. Mater. Sci.* **2013**, *68*, 314.
[29] A. Jain, S. P. Ong, G. Hautier, W. Chen, W. D. Richards, S. Dacek, S. Cholia, D. Gunter, D. Skinner, G. Ceder, K. A. Persson, *APL Mater.* **2013**, *1*, 011002.
[30] K. A. Persson, B. Waldwick, P. Lazic, G. Ceder, *Phys. Rev. B: Condens. Matter Mater. Phys.* **2012**, *85*, 235438.
[31] J. Ribeiro, G. Tremiliosi-Filho, P. Olivi, A. R. de Andrade, *Mater. Chem. Phys.* **2011**, *125*, 449.
[32] M. T. Tang, H. J. Peng, J. H. Stenlid, F. Abild-Pedersen, *J. Phys. Chem. C* **2021**, *125*, 26437.
[33] T. Ludwig, J. A. Gauthier, K. S. Brown, S. Ringe, J. K. Nørskov, K. Chan, *J. Phys. Chem. C* **2019**, *123*, 5999.
[34] J. Le, M. Iannuzzi, A. Cuesta, J. Cheng, *J. Chem. Phys.* **2017**, *146*, 214701.
[35] M. M. Melander, M. J. Kuisma, T. E. K. Christensen, K. Honkala, *J. Chem. Phys.* **2019**, *150*, 041706.
[36] A. H. Larsen, J. J. Mortensen, J. Blomqvist, I. E. Castelli, R. Christensen, M. Dułak, J. Friis, M. N. Groves, B. Hammer, C. Hargus, E. D. Hermes, P. C. Jennings, P. B. Jensen, J. Kermode, J. R. Kitchin, E. L. Kolsbjerg, J. Kubal, K. Kaasbjerg, S. Lysgaard, J. B. Maronsson, T. Maxson, T. Olsen, L. Pastewka, A. Peterson, C. Rostgaard, J. Schiøtz, O. Schütt, M. Strange, K. S. Thygesen, T. Vegge, et al., *J. Phys.: Condens. Matter* **2017**, *29*, 273002.
[37] P. Giannozzi, S. Baroni, N. Bonini, M. Calandra, R. Car, C. Cavazzoni, D. Ceresoli, G. L. Chiarotti, M. Cococcioni, I. Dabo, A. D. Corso, S. de Gironcoli, S. Fabris, G. Fratesi, R. Gebauer, U. Gerstmann, C. Gougoussis, A. Kokalj, M. Lazzeri, L. Martin-Samos, N. Marzari, F. Mauri, R. Mazzarello, S. Paolini, A. Pasquarello, L. Paulatto, C. Sbraccia, S. Scandolo, G. Sclauzero, A. P. Seitsonen, et al., *J. Phys.: Condens. Matter* **2009**, *21*, 395502.
[38] P. Giannozzi, O. Andreussi, T. Brumme, O. Bunau, M. B. Nardelli, M. Calandra, R. Car, C. Cavazzoni, D. Ceresoli, M. Cococcioni, N. Colonna, I. Carnimeo, A. Dal Corso, S. de Gironcoli, P. Delugas, R. A. DiStasio jr, A. Ferretti, A. Floris, G. Fratesi, G. Fugallo, R. Gebauer,

U. Gerstmann, F. Giustino, T. Gorni, J. Jia, M. Kawamura, H.-Y. Ko, A. Kokalj, E. Küçükbenli, M. Lazzeri, et al., *J. Phys.: Condens. Matter* **2017**, *29*, 465901.
[39] K. F. Garrity, K. M. Rabe, J. W. Bennett, D. Vanderbilt, *Comput. Mater. Sci.* **2014**, *81*, 446.
[40] J. P. Perdew, K. Burke, M. Ernzerhof, *Phys. Rev. Lett.* **1996**, *77*, 3865.
[41] J. P. Perdew, K. Burke, M. Ernzerhof, *Phys. Rev. Lett.* **1997**, *78*, 1396.
[42] J. P. Perdew, A. Ruzsinszky, G. I. Csonka, O. A. Vydrov, G. E. Scuseria, L. A. Constantin, X. Zhou, K. Burke, *Phys. Rev. Lett.* **2008**, *100*, 136406.
[43] J. P. Perdew, A. Ruzsinszky, G. I. Csonka, O. A. Vydrov, G. E. Scuseria, L. A. Constantin, X. Zhou, K. Burke, *Phys. Rev. Lett.* **2009**, *102*, 039902.
[44] S. Grimme, J. Antony, S. Ehrlich, H. Krieg, *J. Chem. Phys.* **2010**, *132*, 154104.
[45] C. G. Broyden, *IMA J. Appl. Math.* **1970**, *6*, 76.
[46] R. Fletcher, *Comput. J.* **1970**, *13*, 317.
[47] D. Goldfarb, *Math. Comput.* **1970**, *24*, 23.
[48] D. F. Shanno, *Math. Comput.* **1970**, *24*, 647.
[49] P. N. Plessow, *J. Chem. Theory Comput.* **2018**, *14*, 981.
[50] K. A. Persson, B. Waldwick, P. Lazic, G. Ceder, *Phys. Rev. B: Condens. Matter Mater. Phys.* **2012**, *85*, 235438.
[51] A. K. Singh, L. Zhou, A. Shinde, S. K. Suram, J. H. Montoya, D. Winston, J. M. Gregoire, K. A. Persson, *Chem. Mater.* **2017**, *29*, 10159.
[52] A. M. Patel, J. K. Nørskov, K. Persson, J. H. Montoya, *Phys. Chem. Chem. Phys.* **2019**, *21*, 25323.